GFZ

Helmholtz-Zentrum
POTSDAM

Key Points:
- Doppler shift analysis resolves GNSS reflection events over mountainous topography
- Signal power is retrieved from multipath signatures for water, land, and glacier reflections
- A range of 14 km and more is detected for grazing angle multipath over land

Correspondence to:
L. Peraza and M. Semmling,
mail.luisperaza@gmail.com;
maxsem@gfz-potsdam.de

Analysis of Grazing GNSS Reflections Observed at the Zeppelin Mountain Station, Spitsbergen

L. Peraza[1] , **M. Semmling[1]** , **C. Falck[1]** , **O. Pavlova[2]** , **S. Gerland[2]** , and **J. Wickert[1,3]**

[1]German Research Centre for Geosciences (GFZ), Potsdam, Germany, [2]Norwegian Polar Institute, Fram Centre, Tromsø, Norway, [3]Technische Universität Berlin, Institute of Geodesy and Geoinformation Science, Berlin, Germany

Abstract A reflectometry station has been set up in 2013 near Ny-Ålesund, Svalbard, at 78.9082°N, 11.9031°E. The main goal of the setup is to resolve the spatial and temporal variations in snow and ice cover, based on reflection power observations at grazing elevations. In this study, we develop a method to map the recorded signal power to the main reflection contributions while also discussing the spatial characteristics of the observations. A spectral analysis resolving differential Doppler between direct and reflected signals is presented to identify reflection contributions for a complete year (2014). Strong water reflections are identified with power ratios higher than 70 dB/Hz and constant Doppler shifts of 0.5–0.6 Hz for all elevations. Contributions with ratios higher than 40 dB/Hz can be related to specular land or glacier reflections, for which Doppler shift usually increases with the elevation angle and the distance between reflection point and receiver. Reflections nearby, around 3–5 km, show differential Doppler of 0.4–0.5 Hz, while for reflections farther than 16 km away, Doppler shift is usually larger than 0.8 Hz. Azimuth variations cause cross-track drift of up to 4° during the observation year. Topography-induced shadowing of very low lying satellites limits the extent of the monitoring area. However, the amount of satellites tracked daily, up to 30, allows the reflectometry station to constantly record reflections over areas with thick snow cover and glaciers. This offers the possibility to compare the derived reflected power with local meteorological data to resolve snow and ice variations on the area.

1. Introduction

The use of reflected GNSS (Global Navigation Satellite Systems) signals is currently investigated for various remote sensing applications. Retrievals, today, comprise parameters of the hydrosphere, cryosphere, and biosphere over the ocean and land surface. Prominent ocean examples are the surface wind, e.g., retrieved from TechDemoSat-1 (TDS-1) satellite observations (Foti et al., 2015), the sea surface topography, e.g., based on airborne observation of the GEOHALO mission (Semmling et al., 2014), ocean tides, sea ice coverage, and sea level derived from coastal setups (Anderson, 1999; Fabra et al., 2011; Löfgren et al., 2011; Semmling et al., 2011). Also, a variety of land surface applications were reported including soil moisture (Larson et al., 2008), vegetation coverage (Rodriguez-Alvarez et al., 2011), and snow depth (Ozeki & Heki, 2012; Vey et al., 2016).

Global Navigation Satellite Systems reflectometry is a specific type of radar, where transmitter and receiver are at different locations allowing to observe forward scattered signals. In contrast to backscattered signals, which are used in most conventional radar applications, the GNSS reflection has a much larger range of incidence angles at the scattering surface facet. In the backscatter case, only facets with normal incidence are observed. In the forward scatter case, any facet with specular incidence, i.e., obeying the reflection law can be observed. Assuming a smooth sea surface, facets with normal incidence only occur nadir of the observer. Therefore, a conventional satellite radar altimeter only observes a nadir track. A spaceborne observer of specular GNSS reflections has a significantly larger field of view for ocean altimetry, as recently shown by investigating spaceborne altimetry using GNSS reflection (Semmling et al., 2016; Stosius et al., 2010; Wickert et al., 2016). Even grazing observations with incidence angles >80° are possible and can contain altimetric information, as it was reported by early coastal experiments (Anderson, 1999) and spaceborne studies (Beyerle et al., 2002; Cardellach et al., 2004).

The altimetric use and retrievals to estimate the sea state, sea ice roughness, and concentration have been reported for coastal setups, see, e.g., Fabra et al. (2010) and Semmling et al. (2011, 2012). A mountain setup
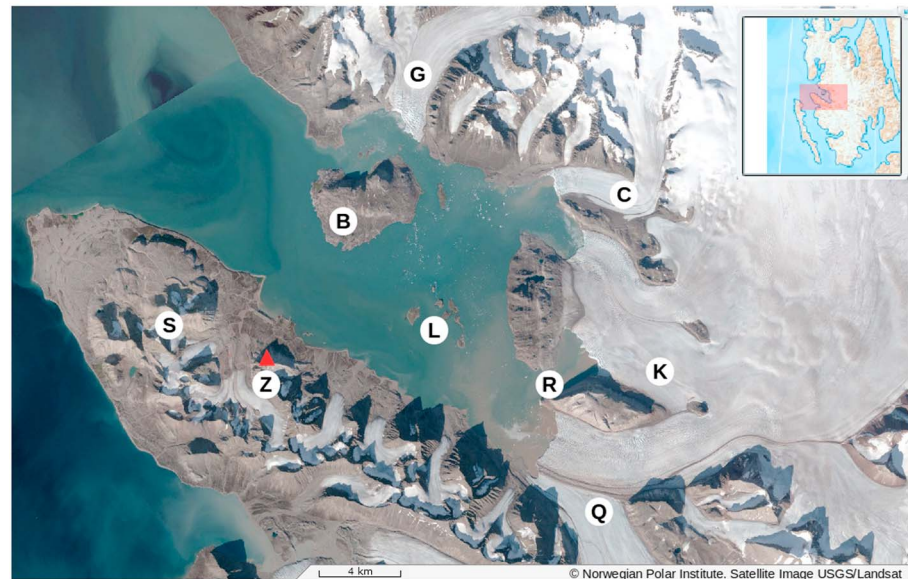
Figure 1. Kongsfjorden and surroundings. Important locations are marked from west to east. S: Schetelig mountain, Z: Zeppelin mountain, B: Blomstrandhalvøya, G: Blomstrandbreen (glacier), L: Lovénøyane archipelago, R: Raudvika, Q: Kronebreen (glacier), C: Conwaybreen (glacier), K: Kongsbreen (glacier). The reflectometry station is marked by the red triangle.

potentially allows to observe glaciers and ice sheets for remote sensing. The fundamental aim of this paper is to map the power of sea and land surface reflections in grazing angle altimetry. The maps, resolved in the satellite's elevation angle and the signal's Doppler shift, shall provide new opportunities to sense the topography and subsurface structure of ice sheets in a grazing angle geometry.

The paper consists of five sections. After this introduction, in section 2, the grazing angle GNSS reflection setup and the data set gathered are described. The characteristics of the observations and the details of the algorithm to retrieve the reflection power are also presented. Using the example event of PRN "(Pseudo Random noise Number)" 15 as case study, the main results of the analysis are outlined in section 3. Section 4 contains a discussion about the monitoring resolution of the reflection power estimates and systematic effects. A summary of the conclusions of this study are provided in the last section.

2. Observations and Models

2.1. Setup and Data Set

The reflectometry setup is located at the Zeppelin mountain station of the Norwegian Polar Institute (NPI), Svalbard. The antenna mounted at 78.9082°N, 11.9031°E has en ellipsoidal height of 511.5 m above WGS-84 and about 475 m above the local sea level of the adjacent Kongsfjorden. It consists of an adapted GNSS receiver known as GORS (GNSS Occultation, Reflectometry and Scatterometry) and two patch antennas (SensorSystems), one up-looking with right-hand circular polarization and one with left-hand circular polarization tilted to the northern horizon.

The antennas have a clear field of view toward the fjord. Figure 1 shows a satellite image mosaic of the Kongsfjorden and all important locations. The water surface of the inner fjord extends on a range of up to 14 km from the station. The visible ice sheet of the eastern glaciers have a range of up to 35 km. The field of view has a width of about 170°, going from the Schetelig mountain in the western direction to the Kronebreen glacier in the eastern direction ([S] and [Q] on Figure 1, respectively). An elevation mask between 2° and 10° is set to focus on grazing elevation reflections. Lower elevation signals are mostly blocked by the surrounding mountains.

The setup records data almost continuously since summer 2013. More than 13,000 h of data are available by now. The data are divided into reflection events of the respective satellites, identified by their PRN. Each event has continuous records of the direct and reflected link to the satellite. The average duration of a reflection event is 22 min, given the used elevation mask. Usually, a rising and a setting event are observed for

each satellite. Data from around 30 GPS satellites are recorded every day, resulting in about 20 h of daily recordings. A filter is applied to use only events that cover the defined elevation range. Events that are interrupted or that do not occur on a daily basis are discarded.

The presented study concentrates on the example event of PRN 15, on its rising arc. This event has a dedicated geometry with potential reflections over the inner fjord and the eastern glaciers. It reaches also potential sea ice areas near the bay Raudvika ([R] on Figure 1), cf. to sea ice maps in Gerland and Renner (2007).

2.2. Observation Type

A GNSS receiver computes a correlation amplitude $a(t)$ of the received signal with the signal replica. For scatterometric applications delay-Doppler maps (DDM) $a(t, \tau, f)$ are computed (Lowe et al., 2002) with a given domain in code delay τ and Doppler shift f close to the expected values τ_s, f_s of the specularly reflected signal.

For grazing angle geometries the effective roughness of the surface decreases and the coherent part of reflected signal increases. A carrier phase sensitive sampling can be introduced

$$
\begin{aligned}
\gamma(t) &= i(t) + iq(t) \\
&= a(t)e^{-i\phi(t)}
\end{aligned}
\tag{1}
$$

where i, q denote in-phase and quadrature samples that are related to $a(t)$ and the residual phase $\phi(t)$ between signal and replica.

The GORS receiver used in the Kongsfjorden setup allows to steer τ, f in order to track the reflected signals if necessary. We demonstrate in this paper that samples of the prompt correlator, tracking the direct signal (Misra & Enge, 2001), can be used to resolve reflections at a rather large distance (>1 km) and grazing elevation angles.

The prompt correlation $\gamma(t, \tau_p, f_p)$ is sampled at 10 Hz with τ_p, f_p being the tracking results for the direct signal's code delay and Doppler shift. Using a series of Fourier transform $\mathfrak{F}\left\{\gamma_p(t)\right\}$ the signal spectrum Γ is resolved for residual Doppler shift f between -5 Hz and 5 Hz

$$
\Gamma(E_n, f) = \left. \mathfrak{F}\left\{\gamma_p(t)\right\}\right|_{E_n}
\tag{2}
$$

where $E_n = E(t_n)$ denotes the elevation angle of the transmitter in the respective time interval $\left\{t_n - \Delta t, t_n + \Delta t\right\}$. Note that the interval is kept small (1 min) to limit changes of E_n (approximately 1°) during this time. An elevation-Doppler map of the signal power is retrieved $\left|\Gamma(E_n, f)\right|^2$ considering Doppler shifts $|f|$ between 0 Hz and 5 Hz. The GORS receiver would allow to retrieve elevation-Doppler maps for both up-looking and horizon-looking antenna links. In this concept study, only maps for the up-looking link with the prompt correlator settings τ_p, f_p are considered. For processing the data, the azimuth and elevation of the transmitters are derived from broadcast orbit products using the GFZRNX software (Nischan, 2016).

2.3. Reflection Model

An early analysis of multipath effects on GPS signal delay is described by Bishop et al. (1985). This early work considers a reflecting facet in a close distance (<1 m) to the receiver antenna. A systematic analysis of GPS multipath using a power spectral mapping is reported by Bilich et al. (2008). In this paper a multipath analysis is performed considering land facets in a distance of up to 30 m around the geodetic station. In the mountain dominated scenario significantly larger distances (> 1 km) occur. A geometric ray tracing allows us to account for the more complex surface. A characteristic quantity is the differential path delay of the reflected ray. It can be modeled, in a general form, as the difference of the reflection path P_1 and the direct signal path P_0.

$$
\rho_j(t) = P_1\left[\vec{x}(t), \vec{s}_j(t), \vec{r}(t), N(t)\right] - P_0\left[\vec{x}(t), \vec{r}(t), N(t)\right]
\tag{3}
$$

The transmitter, receiver positions $\vec{x}, \vec{r}$ determine P_0. The specular point $\vec{s}_j$ is additionally needed for P_1. Only first-order reflections of a ray (P_1) are considered. However, different facets, indicated by index j, may reflect rays in first order at the same epoch t if the reflecting surface is sufficiently complex. In general, the path computation also depends on atmospheric refractivity $N(t)$, which is disregarded in the following geometric ray tracing.
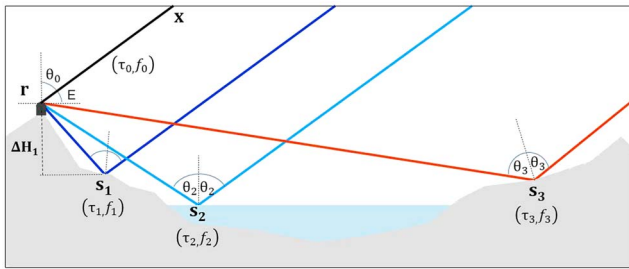
Figure 2. Geometry of GNSS reflections in the Kongsfjorden setup. Rays of the same transmitter are specularly reflected towards the receiver by different surface facets s_j according to their orientations. Three reflections are considered with respective delays τ_j and Doppler shifts f_j. The reflection law applies to the incidence and reflection angles θ_j. The reference link of the direct signal (τ_0, f_0) is also considered. Only for convenient illustration all reflections are depicted in the same plane. In general, different reflection planes will occur. Note also that incidence angles at the receiver and the different reflection points are not equal.

The differential Doppler shift f_j follows from the time derivative $\dot{\rho}_j$

$$f(t) = \frac{1}{\lambda} \dot{\rho}_j \qquad (4)$$

The simplest case considers a reflection facet parallel to the receiver's horizontal plane, cf. Bilich et al. (2008); Semmling et al. (2012). Then the differential path reads

$$\rho(t) = 2 \sin E(t) \Delta H \qquad (5)$$

where ΔH is the perpendicular height difference between antenna and horizontal surface facet. A complex reflection scenario including sea and land surface facets is depicted in Figure 2. It qualitatively describes the setting of the example event PRN 15 at Kongsfjorden.

The specular reflection facets are determined by the ray tracer numerically. The transmitter is described by its azimuth and elevation angle at the receiver position. The surface is given by the digital terrain model with 20 m × 20 m resolution accessible at NPI (2014). The algorithm satisfies the reflection law for the incoming and reflected rays and considers shadowing provoked by the terrain. Based on equation (3), the differential path delay ρ_j is computed and the respective Doppler shift f_j is derived for the specular facets. It has to be noted that the Doppler shift f_j is only defined if the rays keep their specular constellation at $\sim s_j$ for successive epochs.

Assuming an azimuth of 86.5°, typical for the PRN 15 example event, the specular points $\vec{s}_j$ in this direction are determined and plotted with the respective parameters ρ_j, $d\rho_j/dE$ in Figure 3. The modeled example shows that at 4° elevation $\rho_j < 150$ m for all specular points. Reflection signatures will, therefore, be present already in prompt correlation amplitudes (multipath effect). The differential path delay is well within the code correlation limit (300 m). By contrast, signatures at 8° are less probable as corresponding land reflection have a significant larger delay (up to 300 m). Assuming that the constellation does only change in transmitter elevation, i.e., the receiver position and the surface are time invariant, the path rate $d\rho_j/dE$ is the essential geometric parameter to predict the differential Doppler shift, which then read

$$f(t) = \frac{1}{\lambda} d\rho_j/dE \, \dot{E}(t) \qquad (6)$$

the rate $\dot{E}(dE/dt)$ varies between the GPS satellites. Assuming a typical elevation rate of 0.4° per minute, the path rates in Figure 3 correspond to differential Doppler shifts between 0.4 Hz and 2.1 Hz. The differential path is always below 300 m (one chip), so reflection signatures can be expected even without open-loop tracking of the delay. However, delays of more than 150 m occur at rather high-elevation angles, which means that more than half the power is lost without open loop.
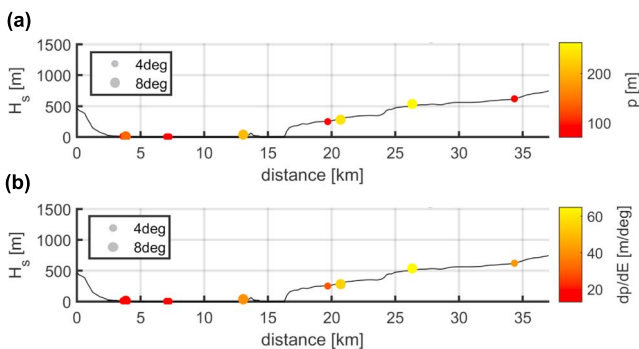
3. Reflection Power Mapping

Two steps are taken in this study to map and identify the reflection signatures in the observation data. The first one is a spectral retrieval to resolve the differential Doppler of the signatures. The use of such Doppler information, e.g., for altimetry, has been reported already (Semmling et al., 2012). In the second step, geometric ray tracing results are used to identify the reflection signatures and assign them to specular surface facets based on the mapping parameters: differential Doppler and transmitter's elevation.

3.1. Spectral Retrieval

Spectral information is retrieved from the signal's Fourier transform $\mathfrak{F}\{x(t)\}$ to resolve the Doppler frequency of specular reflection signatures. From equation (1), complex (in-phase and quadrature) samples given in a discrete

Figure 3. Specular points computed on the surface in eastern direction (86.5° azimuth). (a) The differential path delay and (b) the path delay rate are color coded. Smaller dots refer to 4° elevation angle, larger dots to 8°. Note that not all specular points are shown, only those that lie in the azimuth section.
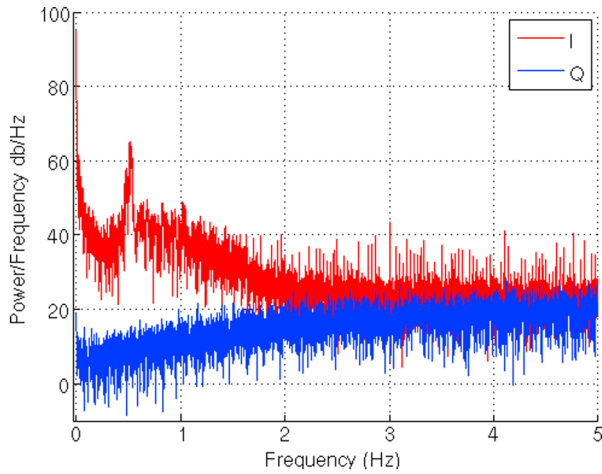
Figure 4. Power spectral density of *I* (red) and *Q* (blue) correlation sum components of PRN 15 samples for complete reflection event on 1 March 2014.
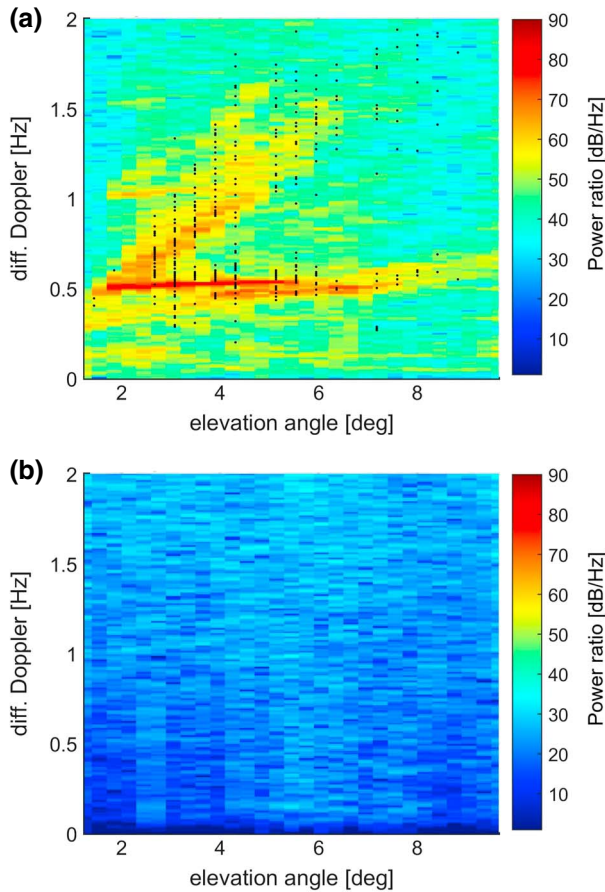

Figure 5. Elevation-Doppler maps of (a) *I* and (b) *Q* correlation sum components of PRN 15 samples on 1 March 2014. The color bar represents derived power ratios in dB/Hz. Main reflection signatures are observed on the map of the In-phase component while the Quadrature-phase contains mostly recorded background noise. Modeled differential Doppler of reflections are plotted as black dots on top of the Elevation-Doppler map of I.

time domain $i(t_j)$ and $q(t_j)$ are taken, where t_j is the respective sample epoch and $j = N$ indicates the last sample of the event. Fourier amplitudes then read

$$I(f) = \mathfrak{F}\{i(t)\}|_k^l$$
$$Q(f) = \mathfrak{F}\{q(t)\}|_k^l . \qquad (7)$$

Spectral power densities $I^2(f)$, $Q^2(f)$ are obtained from the real-valued amplitudes. The indices k, l indicate the first and last samples of the Fourier transform interval. In case of $k = 1$ and $l = N$, spectral information of the entire event is obtained. Figure 4 contains the power spectral density (PSD) for the two components of the selected event (PRN 15) on 1 March 2014. The complete reflection event $\mathfrak{F}\{x(t)\}|_1^N$ is plotted for $f \geq 0$ observed by the reflectometry station, from 0 Hz to 5 Hz.

The differential Doppler f allows to observe the spectral signatures on the recorded signal for the reflection events. Due to the closed-loop nature of the tracking applied, the GORS receiver tracks the master signal amplitude completely in-phase. Hence, the direct and reflected signal power contributions are contained exclusively in the *I* part of the correlation sum. The main contributions, in terms of power, are easily identified according to their spectral distribution. Significant contributions are all stronger than 40 dB and have differential Doppler of less than 1.8 Hz with respect to the direct signal, which is seen as the peak at the zero line ($f = 0$ Hz) of the frequency axis. The second strongest signature is found at around $f = 0.5$ Hz, coming from a specular water reflection, as it will be demonstrated in the next section. Between $f = [0.6 - 1.8]$ Hz, additional contributions significantly affect the shape of the PSD curve. These signatures show strong power for a wider frequency spectrum.

The *Q* component's PSD has a much lower power level (<20 dB) and is considered as an estimate of the background noise. There is an increase in noise power from about 10 dB at 1 Hz to ~20 dB at higher frequencies roughly matching the power levels observed on the I part of the signal at the same frequencies. A similar behavior was encountered for the PSD plots of the other events observed during the campaign. All power ratios are shown in dB/Hz for visualization convenience using $p[\text{dB/Hz}] = 10\log_{10}(\Gamma^2_1/\Gamma^2_0)$ were Γ^2_1 is the magnitude squared of the corresponding Fourier coefficients ($I^2(f)$ or $Q^2(f)$) and $\Gamma^2_0 = 1$. Small p is used to define power ratios in dB/Hz to avoid confusion with variable P used to denote the ray paths.

3.2. Mapping Results

The differential Doppler behavior of a reflection event can be represented for all elevations of a transmitter as an elevation-Doppler map. If the interval length $t_l - t_k$ in equation (7) is reduced, e.g., to 1 min, and $\mathfrak{F}$ is applied sequentially, time-resolved spectral information is retrieved. As the elevation change rate $\dot{E}$ is almost constant during typical events, for the case of this study, the time-resolved spectra provides the elevation-Doppler maps of *I* and *Q*. In Figure 5 the maps of the samples of PRN 15 are shown. These have a resolution of 0.4° in the elevation domain ($t_l - t_k = 1$ min) and of 0.01 Hz in the frequency axis and are color coded according to signal power in dB/Hz. The frequency axis is plotted between 0 and 2 Hz to ease visualization of relevant contributions. The main signatures observed on the PSD plots on Figure 4 can be also identified in Figure 5, now broken down per elevation angle. The strongest contribution seen in the I's elevation-Doppler map (Figure 5a) is again, besides the direct signal at $f = 0$ Hz, the specular reflections consistently between $f = [0.5:0.6]$ Hz, present at almost all elevations. The constant differential Doppler values as the transmitter's elevation changes occur due to the mirror-like conditions of the fjord's water surface. The differential path
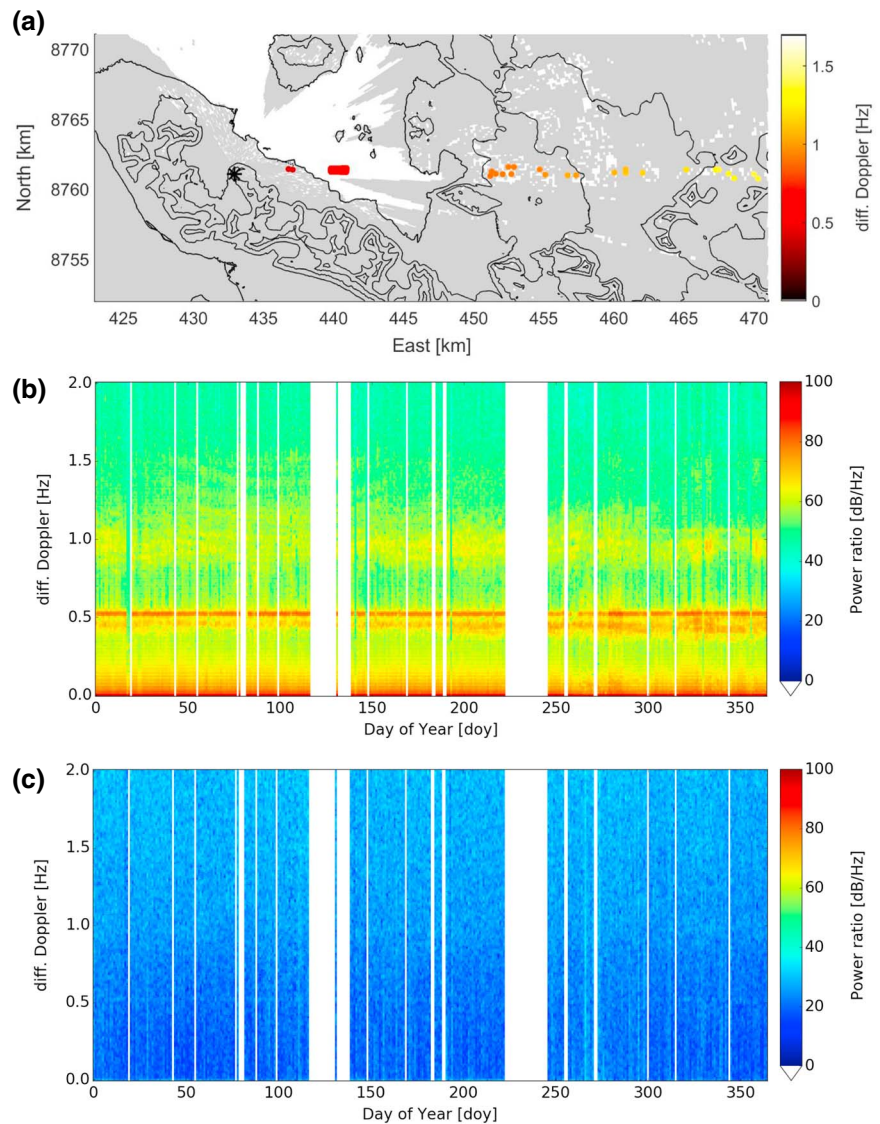
Figure 6. Differential Doppler behavior of eastern event of PRN 15 at $E = 4°$. (a) Map of Kongsfjorden with location of reflections points for event on 1 March 2014; contour lines with 200 m height resolution are drawn. Gray areas mark topographic shadowing of signals from transmitters below $E = 4°$. (b and c) Differential Doppler behavior for year 2014 from I and Q samples, respectively. Surface facet orientations determine the Doppler residuals of the reflection with respect to the direct signal. Reflections from water show constant differential Doppler of around $f = 0.5-0.6$ Hz. Land reflections closer to the receiver show values of around $f = 0.4-0.5$ Hz, while reflections farther away, around >16 km from the receiver's location, have much larger differential Doppler that is related to the larger differential path of the rays $f > 0.8$.

between direct and reflected links from a transmitter at different positions varies only slightly (as seen in Figure 3) over this area.

On the contrary, the differential Doppler for signatures other than the detected water surface reflections varies with the elevation angle. The f range of these reflections is seen in the elevation-Doppler map of I as ascending linear signatures between $f = [0.6:1.6]$ Hz, which also appear on the I's PSD on Figure 4. Another strong contribution is found starting from $E = 3°$ and continuing until approximately $E = 8°$. These signatures have differential Doppler that vary only slightly, $f = [0.4-0.5]$ Hz, and are smaller in magnitude than those of the reflections of water. Further signatures are observed above $f = 1$ Hz up to around $f = 1.8$ Hz.

Higher-order harmonics of sea surface signature at 0.5 Hz are visible at about 1.0 Hz and 1.5 Hz. These harmonics are restricted to lowest elevation angles and may be caused by multipath related filter settings of the receiver.
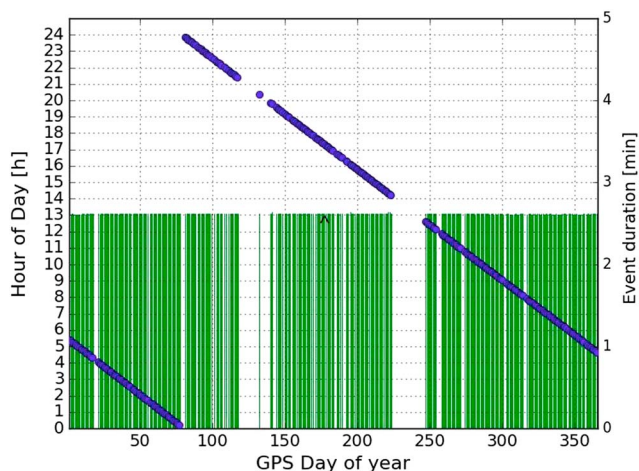
Figure 7. Time of occurrence and duration of reflections within bin at 4° of PRN 15 for the year of 2014.

3.3. Ray Tracing Results

Using the ray tracing model in equation (6), the reflections are mapped by the corresponding transmitter's elevation angle at the recording time. To do this, the reflection event resolution in the elevation domain was reduced to 1° bins with $t_l - t_k = 2.5$ min, cf. equation (7). A bin is defined to contain the integrated contributions within $E \pm 0.5°$, having E being the range of integers within the elevation window used (2–10°). A reflection event is then divided into nine elevation bins of 1° each.

A subset of the sample observations is geographically mapped in Figure 6a. The subset corresponds to the observations within bin at $E = 4°$, color coded by their f by which they can also be traced on the elevation-Doppler maps on Figure 5. The plot allows to observe the differential Doppler behavior at specific positions of the satellite as well as the relation to the distance between the reflection point and the receiver. Easily identifiable are the detected reflections from the water surface of Kongsfjorden, which are plotted as dark red circles. The additional reflections can now be distinguished as land surface reflections. For this example event, the location of the land reflections varies greatly. Reflections occur in the surrounding 3–5 km from the receiver's position as well as more than 16 km away over Kongsbreen. The differential Doppler is seen to increase with the distance between reflection point and receiver. The nearby land reflections appear in the plot as darker red circles just by the coastline. These areas are easily flooded, so differential Doppler observations might correspond equally to water and land surface facets which explains why f values are similar to the water reflections over the fjord. The signatures located further away cover a larger area and were able to be recorded given the sloped topography of the terrain, which faces toward the receiver direction. The differential Doppler vary significantly, $f = [0.8–1.5]$, due to the increased path length of the radio links at more distant locations. These are reflection from land and glacier/ice surface facets.

Figures 6b and 6c contain the differential Doppler of the sample bin observed during the complete year of 2014 for both components of the correlation results. All of the specular contributions discussed previously are tracked consistently throughout the year, seen on the I plot (Figure 6b). The water reflections as well as the nearby land reflections occurring by the Kongsfjorden are described by the two, sharply defined, red signatures around $f = 0.5$ Hz. The Kongsbreen reflections, spanning over a larger frequency spectrum, occur at ∼1 Hz. The Q component's plot for this bin shows a constant noise level.

4. Monitoring Resolution and Systematic Effects

Due to the geometry of the GPS orbits, the reflection of a specific satellite occurs roughly over the same area of the Earth every day with small variations in the azimuth domain, as shown in Beyerle and Zus (2017). Moreover, as the satellite ascends or descends in its orbit, the specular reflection point moves closer to, or farther away from, the receiver's position along a track that covers different areas. The temporal and spatial variations of the reflection tracks as well as the systematic effect induced by land topography and atmospheric refraction are discussed in the following section.

4.1. Temporal Resolution

The continuous tracking of the reflection of all available satellites shows the monitoring capabilities of the reflectometry station. Figure 7 displays the temporal coverage of the integrated observations at sample bin $E = 4°$ of PRN 15. The left axis of the figure refers to the average time of occurrence (in hour of day) of the observations, shown as blue circles. Reflections for this bin occur around 4 min earlier every day, which adds up to roughly 24 h a year, having the cycle start again on day of year (DOY) 84. The right axis of the plot represents the duration of the bin in minutes. The reflections last approximately 2.5 min each day, which is similar for all bins. The constant duration shows that the receiver was able to track the satellite throughout its entire pass at the specific elevation almost every day. Gaps represent days with interrupted or nonexisting observations, in agreement with Figure 6. Site maintenance and hardware problems caused measurement interruption during the months of May and August 2014, respectively.

Table 1
Azimuth Variation of Events Occurring on Water Surface

PRN	Mean azimuth (deg)	SD (deg)	Width (m)	$\dot{E}$ (°/min)
1	*346.89*	*±0.05*	*34.89*	*0.38*
2	*45.74*	*±0.77*	*311.70*	*0.40*
3	*0.73*	*±0.54*	*133.34*	*0.37*
7	*354.51*	*±0.98*	*369.15*	*0.39*
10	*357.81*	*±0.51*	*240.57*	*0.37*
11	*352.78*	*±0.61*	*260.53*	*0.35*
15	*9.01*	*±1.09*	*412.89*	*0.37*
19	*358.98*	*±0.92*	*367.90*	*0.38*
21	*358.70*	*±1.09*	*402.89*	*0.37*
22	*344.92*	*±1.00*	*396.64*	*0.37*
23	*6.99*	*±0.47*	*115.89*	*0.37*
24	*342.69*	*±0.95*	*349.16*	*0.37*
26	*346.80*	*±0.40*	*160.76*	*0.39*
27	*349.39*	*±0.05*	*36.13*	*0.38*
28	*338.72*	*±0.13*	*58.56*	*0.39*
1	64.72	±0.07	61.06	0.38
7	86.57	±0.96	369.15	0.42
10	76.69	±0.57	270.52	0.38
11	67.79	±0.78	329.18	0.35
14	45.91	±0.52	240.57	0.41
15	88.44	±1.25	494.21	0.38
17	47.58	±1.02	360.41	0.41
18	63.70	±0.07	16.20	0.40
19	78.90	±0.99	392.89	0.39
22	79.48	±1.10	435.40	0.40
24	59.77	±0.97	367.90	0.37
25	47.38	±1.06	419.14	0.38
26	67.32	±0.38	167.00	0.39
27	67.57	±0.12	68.53	0.36
28	70.50	±0.12	56.07	0.41

Note. Setting events are in italics. Mean azimuth is independent of the elevation of the transmitter. However, the width or extent of the cross-track drift per PRN is not. The width values are calculated for observations within bin at $E = 4°$ using a mean distance between reflection point and receiver of 7.14 km. Last column shows the elevation rate $\dot{E}$ in °/min also at $E = 4°$.

4.2. Cross-Track Variations

The cross-track dimensions, or width, of the observed areas is determined by the azimuth variations of the transmitter. These variations depend on the satellite orbit. The ground track can have a particular cross-track drift over the year. Table 1 lists the azimuth angle characteristics of all the events from water reflections collected during 2014. The mean azimuth and its standard deviation are given. Also included is the maximum cross-track drift, in meters, during the complete year for bins at $E = 4°$ of each event. This value depends on the elevation angle of the transmitter and it increases with the distance between reflection point and receiver. The table contains only events from satellites whose azimuth variations remained within the $±10°$ range.

Azimuth drift for the selected events during 2014 is less than 5°. However, those values affect differently the cross-track size of the surfaces observed, depending on the elevation of the satellite. The cross-track drift of PRN 15 at 4° of elevation shifts the track by a distance of ∼500 m over the year. This distance reaches about 1 km for elevations of 2°.
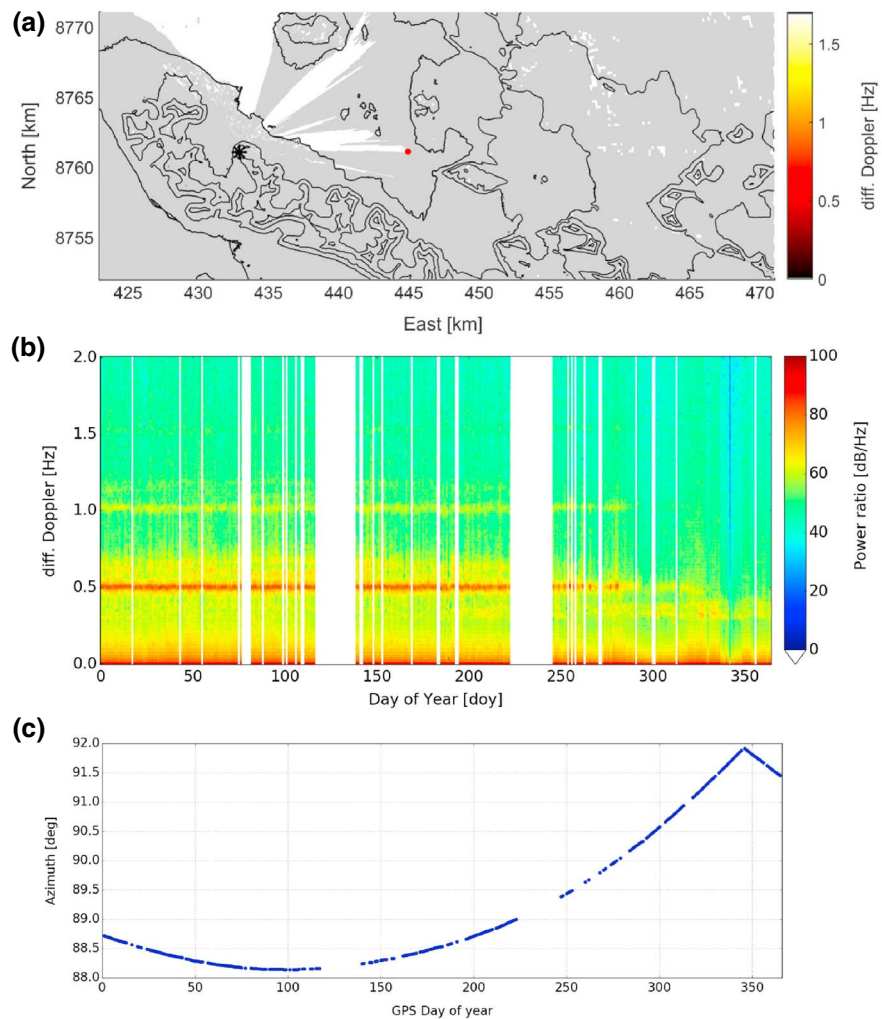
Figure 8. Cross-track drift due to azimuth angle variations of GNSS transmitters, case study PRN 15. (a) Geographic plot of the modeled reflections of event on 1 March 2014 at $E = 2°$ color coded by differential Doppler, the gray mask shows the topographic shadowing of signals from satellites below such elevation. (b) Differential Doppler measured during the analyzed year for the same reflections. (c) Azimuth angle drift observed for the same samples. The shadowing areas are estimated using a model that takes as input the height of the terrain and orbital information of transmitters at $E = 2°$. The signal disappears when the reflection enters the shadow. For instance, the observations at $E = 2°$ of PRN 15 are shadowed when the satellite's orientation is >90° after DOY 280.

4.3. Topographic Effects

Mountains in the northern and eastern direction cast a significant shadow on the fjord surface. The ray tracing tool was used to estimate the shadowed areas over the terrain for transmitters at different elevations. The results for elevations 2° and 4° are added as gray layers to the terrain plots in Figures 6a and 8a, respectively. In Figure 8 it can be seen how specular water reflections occur on a gap or opening between the shadows of the mountains located farther east of the receiver. Figure 8b contains the differential Doppler for the event during the complete year. The strong signatures around $f = 0.5$ Hz, water reflections, were constantly monitored for most of the campaign. At around DOY 280, when the transmitter's azimuth surpassed the ~90°, as seen on the azimuth variation plot (Figure 8c), the reflection power fades. When drifting to azimuth higher than ~90° the event enters the shadow of the Colletthøgda mountain in between Kongsbreen and Kronebreen glaciers (see Figure 8a).

4.4. Refractivity Effects

The ray tracing performed to calculate the specular reflection facets on the terrain disregards atmospheric refraction so far. The reason is the correlation between specular point position and atmospheric bending
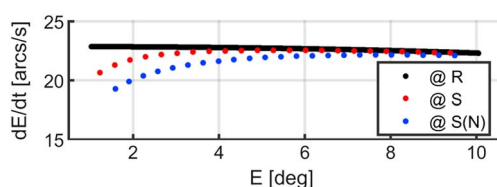
Figure 9. Comparison of changes in the elevation range $\dot{E}$ for PRN 15 event on 1 March 2014 under different assumptions: considering the elevation angle of transmitter at receiver position, R; considering elevation angle at (previously calculated) specular point, S; and considering the elevation angle at specular point taking atmospheric refraction into account, $S(N)$.

which would require a complex iteration accounting for both terrain geometry and atmospheric refraction. In case of the ellipsoidal sea surface a ray tracing solution considering geometry and atmosphere has been found (Semmling et al., 2012). It is used here to estimate the refractive bias on path delay-Doppler shift and to quantify the bending effect at least for sea surface reflection points.

Considering the reflection points found on the sea surface in Figure 3 for 4° and 8° elevation, path delay biases of 5.2% and 2.0% and Doppler shift biases of −2.7% and −0.1% are found, respectively. The elevation rate and the elevation angle are recalculated at the specular sea surface point. The elevation rate values are plotted versus the elevation angle in Figure 9 where they are compared with the values at the receiver position, considered so far. The plot shows a geometric effect comparing the curves for the receiver position R (black) and the geometric specular point S (red). It also shows a clear bending effect comparing the curves for the geometric specular point S (red) and the refraction corrected point $S(N)$. In a future study, strategies have to be found to correct the atmospheric delay and ray bending also for reflection facets over complex terrain.

5. Conclusions

We conclude from this study that a spectral analysis of GNSS samples reveal reflection signatures in considerable distances (>10 km) without a dedicated reflection tracking. A geodetic receiver providing 10 Hz samples of the signal's in-phase amplitude or signal-to-noise ratio is sufficient. A precondition is a ground-based setup, e.g., on a mountain, with the dedicated scene in view at grazing elevations angles.

It has been shown in the paper that mapping the signal's spectrum in an elevation-Doppler map allows to distinguish different reflection signatures by elevation angle and Doppler shift. In contrast to the established concept delay-Doppler maps, the elevation-Doppler map relies on a single correlator sampling. To resolve the Doppler shift from the single set of samples coherent reflections are required. The concept is especially suitable for a grazing geometry where the effective surface roughness is small and coherent reflection can be expected.

The ray tracing calculations confirm that sea surface reflections in a distance between 5 and 12 km can be observed as well as glacier surface reflections in distances of more than 14 km. The mapped differential Doppler shift contains altimetric information which has been exploited for sea surface altimetry in previous studies already. It is an important challenge for upcoming studies to develop an altimetric inversion also to resolve height changes of glaciers or ice sheets.

A difficulty that has to be addressed in this respect is to account for atmospheric delay and ray bending. The further development of ray tracing algorithm that is adapted to surface topography is essential for this purpose. A limitation for land surface monitoring, in general, arises from the successive azimuth drift of recurring satellites. It prevents ongoing monitoring of the same reflection track as the reflection point is shifted considerably during this drift. The high and still increasing number of GNSS transmitters can perspectively mitigate this problem. A dense coverage of reflection tracks will allow a reasonable revisit time also for drifting tracks.

References

Anderson, K. D. (1999). Determination of water level and tides using interferometric observations of GPS signals. *Journal of Atmospheric and Oceanic Technology*, *17*, 1118–1127.

Beyerle, G., & Zus, F. (2017). Open-loop GPS signal tracking at low elevation angles from a ground-based observation site. *Atmospheric Measurement Techniques Discussion*, *10*, 15–34. https://doi.org/10.5194/amt-10-15-2017

Beyerle, G., Hocke, K., Wickert, J., Schmidt, T., Marquardt, C., & Reigber, C. (2002). GPS radio occultations with CHAMP: A radio holographic analysis of GPS signal propagation in the troposphere and surface reflections. *Journal of Geophysical Research*, *107*(D24), 4802. https://doi.org/10.1029/2001JD001402

Bilich, A., Larson, K. M., & Axelrad, P. (2008). Modeling GPS phase multipath with SNR: Case study the Salar de Uyuni, Boliva. *Radio Science*, *113*, B04401. https://doi.org/10.1029/2007JB005194

Bishop, G. J., Klobuchar, J. A., & Doherty, P. H. (1985). Multipath effects on the determination of absolute ionospheric time delay from GPS signals. *Radio Science*, *11*, 388–396.

Cardellach, E., Ao, C. O., de la Torre Juarez, M., & Hajj, G. A. (2004). Carrier phase delay altimetry with GPS-reflection/occultation interferometry from low Earth orbiters. *Geophysical Research Letters*, *31*, L10402. https://doi.org/10.1029/2004GL019775

Fabra, F., Cardellach, E., Nogues-Correig, O., Oliveras, S., Ribo, S., Rius, A., . . . d'Addio, S. (2010). Monitoring sea-ice and dry snow with GNSS reflections. In *Proceedings of IEEE International Geoscience and Remote Sensing Symposium (IEEE-IGARSS)* (pp. 3837–3840). Piscataway, NJ: IEEE.

Fabra, F., Cardellach, E., Rius, A., Ribó, S., Oliveras, S., Belmonte, M., . . . D'Addio, S. (2011). Phase altimetry with dual polarization GNSS-R over sea ice. *IEEE Transactions on Geoscience and Remote Sensing*, *50*(6), 2112–2121. https://doi.org/10.1109/TGRS.2011.2172797

Foti, G., Gommenginger, C., Jales, P., Unwin, M., Shaw, A., Robertson, C., & Roselló, J. (2015). Spaceborne GNSS reflectometry for ocean winds: First results from the UK TechDemoSat-1 mission. *Geophysical Research Letters*, *42*, 5435–5441. https://doi.org/10.1002/2015GL064204

Gerland, S., & Renner, A. H. H. (2007). Sea-Ice mass-balance monitoring in an Arctic fjord. *Annuals of Glaciology*, *46*, 435–442.

Larson, K. M., Small, E. E., Gutmann, E. D., Bilich, A. L., Braun, J. J., & Zavorotny, V. U. (2008). Use of GPS receivers as a soil moisture network for water cycle studies. *Geophysical Research Letters*, *35*, L24405. https://doi.org/10.1029/2008GL036013

Löfgren, J. S., Haas, R., & Johansson, J. M. (2011). Monitoring coastal sea level using reflected GNSS signals. *Advances in Space Research*, *47*, 213–220.

Lowe, S. T., Kroger, P., Franklin, G., LaBrecque, J. L., Lerma, J., Lough, M., . . . Young, L. E. (2002). A delay/Doppler-mapping receiver system for GPS-reflection remote sensing. *IEEE Transactions on Geoscience and Remote Sensing*, *40*(5), 1150–1163. https://doi.org/10.1109/TGRS.2002.1010901

Misra, P., & Enge, P. (2001). *Global Positioning System — Signals, Measurements, and Performance*. MA: Ganga-Jamuna Press, Lincoln.

Nischan, T. (2016). GFZRNX-RINEX GNSS data conversion and manipulation toolbox (version 1.05), GFZ Data Services. Potsdam, Germany: German Research Centre for Geosciences (GFZ) https://doi.org/10.5880/GFZ.1.1.2016.002

NPI (2014). Terrengmodell Svalbard (S0 Terrengmodell) Norwegian Polar Institute. Tromsø, Norway: Fram Centre.

Ozeki, M., & Heki, K. (2012). GPS snow depth meter with geometry-free linear combinations of carrier phases. *Journal of Geodesy*, *86*, 209–219. https://doi.org/10.1007/s00190-011-0511-x

Rodriguez-Alvarez, N., Bosch-Lluis, X., Camps, A., Aguasca, A., Vall-llossera, M., Valencia, E., . . . Park, H. (2011). Review of crop growth and soil moisture monitoring from a ground-based instrument implementing the Interference Pattern GNSS-R Technique. *Radio Science*, *46*, RS0C03. https://doi.org/10.1029/2011RS004680

Semmling, M., Beyerle, G., Stosius, R., Dick, G., Wickert, J., Fabra, F., . . . d'Addio, S. (2011). Detection of Arctic Ocean tides using interferometric GNSS-R signals. *Geophysical Research Letters*, *38*, L04103. https://doi.org/10.1029/2010GL046005

Semmling, M., Schmidt, T., Wickert, J., Schön, S., Fabra, F., Cardellach, E., & Rius, A. (2012). On the retrieval of the specular reflection in GNSS carrier observations for ocean altimetry. *Radio Science*, *47*, RS6007. https://doi.org/10.1029/2012RS005007

Semmling, M., Beyerle, G., Beckheinrich, J., Ge, M., & Wickert, J. (2014). Airborne GNSS reflectometry using crossover reference points for carrier phase altimetry. In *Proceedings of the IEEE International Geoscience and Remote Sensing Symposium (IGARSS)*, Quebec City, QC, Canada, pp. 3786–3789. https://doi.org/10.1109/IGARSS.2014.6947308

Semmling, M., Leister, V., Saynisch, J., Zus, F., Heise, S., & Wickert, J. (2016). A phase-altimetric simulator: Studying the sensitivity of Earth-reflected GNSS signals to ocean topography. *IEEE Transactions on Geoscience and Remote Sensing*, *54*(11), 6791–6802. https://doi.org/10.1109/TGRS.2016.2591065

Stosius, R., Beyerle, G., Helm, A., Hoechner, A., & Wickert, J. (2010). Simulation of space-borne tsunami detection using GNSS-Reflectometry applied to tsunamis in the Indian Ocean. *Natural Hazards and Earth System Science*, *10*(6), 1359–1372.

Vey, S., Güntner, A., Wickert, J., Blume, T., Thoss, H., & Ramatschi, M. (2016). Monitoring snow depth by GNSS Reflectometry in built-up areas: A case study for Wettzell, Germany. *IEEE Selected Topics in Applied Earth Observations and Remote Sensing*, *9*(10), 4809–4816. https://doi.org/10.1109/JSTARS.2016.2516041

Wickert, J., Cardellach, E., Bandeiras, J., Bertino, L., Andersen, O., Camps, A., . . . Zuffada, C. (2016). GEROS-ISS: GNSS reflectometry, radio occultation and scatterometry onboard the International Space Station. *IEEE Selected Topics in Applied Earth Observations and Remote Sensing*, *9*(10), 4552–4581.